



Contents lists available at SciVerse ScienceDirect

Cold Regions Science and Technology

journal homepage: www.elsevier.com/locate/coldregions

Rigid obstacle impacted by a supercritical cohesive granular flow using a 3D discrete element model

Lionel Favier ^{a,*}, Dominique Daudon ^b, Frédéric-Victor Donzé ^b^a Laboratoire de Glaciologie et Géophysique de l'Environnement (LGGE), CNRS, UJF-Grenoble, BP 96, 38402 Saint-Martin-d'Hères Cedex, France^b Université Joseph Fourier, Grenoble University/Grenoble INP/CNRS, 3SR Laboratory, Grenoble F-38401, France

ARTICLE INFO

Article history:

Received 7 March 2012

Accepted 19 September 2012

Available online xxxx

Keywords:

Cohesive granular flow
Flow/obstacle interaction
Drag coefficient
Contact network
Discrete element model
Wet-snow avalanches

ABSTRACT

This study examines the drag coefficient of an obstacle impacted by a 3D cohesive granular flow using a discrete element model. A specific numerical setup is used to carry out reproducible and controlled normal impact simulations, in which the upstream flow properties are fully controlled parameters. The micromechanical contact model involves the physical properties of friction, normal elastic–plastic repulsion, dissipation, and a normal cohesion factor that induces bulk cohesion in the granular assembly. The effect of cohesion on the obstacle load is investigated through a micro-scale analysis. We show that increasing the cohesion leads to an increase of the obstacle drag, through a densification of the contact network, which enhances the transmission of contact forces to the obstacle. This experiment is extended to a wide range of supercritical flows, with Froude numbers between 1.5 and 11.2. The resulting drag coefficient curves are represented as power law functions of the Froude number. We then demonstrate the dependency of the power law exponent on the ratio between inertia and gravitational forces. Our results suggest that the assessment of drag coefficient critical values by conventional avalanche protection guidelines could be improved by a mechanical consideration of cohesion for certain snow types.

© 2012 Elsevier B.V. All rights reserved.

1. Introduction

The design of passive protection structures against snow avalanches requires an estimation of the drag coefficient, which is based on a simple static relationship between the impact pressure and the inner flow kinetic energy. Due to the lack of knowledge on the interaction between an avalanche and an obstacle, i.e. how the upstream flow is disturbed, and what the consequence is on the obstacle load, protection structure designers adopt drag coefficients that are simply based on the geometrical properties of the structure, and on the flow regime. For example, the Swiss guidelines recommend to use 1 or 2 for small round-shape or square-shape obstacles, respectively (Salm et al., 1990). Based on impact pressure measurements made at the Ryggfönn test site (Norem, 1990), the Norwegian guidelines recommend to use drag coefficients from 2.5 to 6.3 depending on the snow moisture content. An attempt to standardise all these recommendations was made by the European Commission in Barbolini et al. (2009).

The first substantial studies investigating the pressure exerted by snow avalanches on a structure were performed by Voellmy (1955), Mellor (1968) or Shen and Roper (1970). The avalanche was assumed to behave as a steady stateflow and the impact pressure was initially formulated as a function of the squared velocity only, before the

addition of a flow density term based on deposition zone data analysis (Schaerer, 1973). In order to get realistic data, full-scale experiments on snow avalanches were also performed. The pressure was measured by load cells fixed on a supporting structure immersed within the avalanche (McClung et al., 1985; Nishimura et al., 1993; Schaer and Issler, 2001). More recently, in-situ experiments were also performed by Sovilla et al. (2008a,b) at the Vallée de la Sionne test site, and by Gauer et al. (2007) at the Ryggfönn test site. Based on a possible influence of the supporting structure on the pressure recorded by load cells, a different approach was to investigate the impact pressure by inverse analysis of the deformations of an avalanche-scale structure (Berthet-Rambaud et al., 2008; Thibert et al., 2008).

The calculation of the drag coefficient requires to know the temporal evolution of the drag force, the inner flow density and velocity. In Thibert et al. (2008), the density is assumed to increase linearly over time between densities measured in the starting zone and in the deposition zone, but this method involves important major uncertainties since the bulk density is more a function of the Froude number, the first decreasing while the latter increasing. In the same publication, the velocity is estimated from surface velocity, whereas inner and surface dynamics can be fairly different (Jop et al., 2005). All these sources of errors contribute to add uncertainties to the resulting drag coefficient.

Because in-situ measurements are complex, the hypothesis of snow avalanches behaving much like granular flows is increasingly

* Corresponding author. Tel.: +33 4 76 82 42 10.

E-mail address: Lionel.Favier@lgge.obs.ujf-grenoble.fr (L. Favier).

used to study this complex natural phenomenon in the laboratory or with numerical simulations. Snow is a complex granular material which evolves over time with respect to snow metamorphism thermodynamical laws (Rognon et al., 2008a). Therefore, a wide variety of snow grain shapes, sizes and mechanical properties co-exist within the snow cover. The geometrically complex grains of newly deposited fresh snow rapidly transform into more dense and smaller spherical grains, stuck together through the sintering process which forms small ice bonds between grains. When temperature rises above the melting point, ice bonds and grain surfaces melt, grains grow to reach a few millimetres and are linked by capillary cohesion. The deposit of a snow avalanche is composed of snow balls. Their typical size is in the order of a few centimetres, as shown by De Biagi et al. (2012) using a fractal approach, and seems to evolve as an increasing function of the moisture content, as shown by Bartelt and McArdell (2009). These snow balls were formed within the dense part of the rapid shear flow of the avalanche. Small-scale in-situ investigations (Rognon et al., 2008a) made on dry natural snow have also identified a typical size of a few centimetres.

It is not well known how the bulk cohesion influences the impact pressure of snow avalanches. Recently, really high values of the drag coefficient, up to 5 times the maximum value of 6 recommended by Norem (1990), were obtained from analysis of snow avalanches performed by Sovilla et al. (2008a, 2010) and Baroudi et al. (2011). The authors explain this by the presence within the snow avalanche of force chains (Sovilla et al., 2010). For example, the formation and destruction of such force chains were identified as a possible cause of the high impact load fluctuations in the case of wet-snow avalanches (Baroudi et al., 2011). The presence of force chains seems to be related to the flow density (Geng and Behringer, 2005), which is a decreasing function of the vertical shearing which itself is higher for rapid dry avalanches. For plug-flow like avalanches with a Froude number around 1, the low amount of shearing seems to facilitate the formation of force chains due to capillary cohesion.

Using this analogy between snow avalanches and granular flows, small-scale laboratory experiments have been performed to study granular flows impacting obstacles (Faug et al., 2011; Hauksson et al., 2007; Ma et al., 2009; Platzer, 2006; Valentino et al., 2008). This approach is useful to develop controlled experiments in which quantities can be measured in a reproducible manner, as for example velocity in Barbolini et al. (2005). However, the drag coefficient depends on quantities such as density and velocity within the flow. The experimental approach cannot provide this information because a sensor inserted in the flow disturbs the flow characteristics. Numerical approaches, on the other hand, can provide all the parameters needed to compute the drag coefficient, but these models have to agree with experimentation in order to be reliable, as done by Moriguchi et al. (2009) using a continuum method, or by Teufelsbauer et al. (2011) using a discrete method.

So far, studies on the influence of the Froude number Fr on the obstacle drag coefficient C_d are sparse. Some of them cover a wide range of Froude number. Thibert et al. (2008), Baroudi and Thibert (2009) performed in-situ avalanche experiments for Froude numbers between 0.5 and 7. Chehata et al. (2003) performed laboratory experiments on granular flows impacting a round-shape obstacle in a wide range of subcritical regimes. Both research groups established a relationship between the drag coefficient as a power law function, such as $C_d = aFr^{-b}$. The first group obtained a b value between 1.2 and 1.3, and the second obtained a b value of 2, which shows that the velocity does not influence the drag coefficient for subcritical regimes.

In this paper, we study the drag coefficient of an obstacle impacted by a supercritical cohesive granular flow for a wide range of Froude numbers, using a discrete approach. A specific numerical tool based on a discrete element method is set up to compute the drag coefficient from fully controlled flow parameters. The first two sections are dedicated to the description of the model, Section 2 for the contact

model, and Section 3 for the setup of the numerical tool. Section 4 gives the results obtained with the numerical model. It is subdivided into two parts, the first one showing that cohesion contributes to increase the drag coefficient through a densification of the contact network in the granular flow, the second extending the first one to a wide range of supercritical flow regimes.

2. The discrete numerical model

The granular flow experiments were modelled with a discrete element method called Molecular Dynamics (first formulated by Cundall and Strack (1979)), implemented in the open-source code YADE¹ (presented in Kozicki and Donzé (2008)). A Molecular Dynamics simulation is started by first generating an assembly of discrete elements, which are used to represent both, fixed “boxes” and moving “particles”. The contact forces between elements are then computed according to the contact model (see the following Section), considering a normal and a tangential contribution for each binary contact. Newton’s second law is applied to each particle to determine its resulting acceleration, which is time integrated to obtain the updated particle velocity and position. This process is repeated until the simulation is over. All elements have a fixed geometry, particles are spherical and boxes are parallelepipedic.

2.1. Description of the contact model

Two elements are in contact when there is an overlap between them, which means that the distance between their centroids is lower than the sum of their two radii. The contact force is computed by applying the contact model to the relative displacement and velocity between the two contacting elements. The contact force is composed of the normal force and the tangential force (represented in Fig. 1), which are described by the normal (see Fig. 2) and the tangential (see Fig. 3) contact models respectively.

2.1.1. Normal contact: Linear hysteretic cohesive model

The normal contact force F_n is described by the piecewise elastic² hysteretic cohesive model, shown in Fig. 2. This model was initially proposed by Walton and Braun (1986) in its non-cohesive version, and extended by Luding et al. (2005) and Luding (2008) to include a cohesive behaviour to account for the sintering process. The normal contact model represents successively a linear repulsive loading phase (state 1) followed by an unloading process made up of a repulsive phase (state 2) and two successive attractive phases (state 3 and state 4). Whatever the state, the evolution of the normal force falls into a straight line for which the slopes are k_n^1 for the first state, k_n^2 for both the second and third states, and k_n^3 for the fourth one. The values of stiffnesses k_n^i ($i = 1, 2, 3$) are uniform and constant for the duration of each simulation. However, the normal contact model extrema, i.e. F_n^{max} for the repulsive part and F_n^{oh} for the attractive part (see Fig. 2), depends also on the initial relative velocity of the two contacting elements, which can decrease or increase depending on whether additional energy is supplied by external elements impacting this prior binary contact.

A mathematical description of the normal contact model is provided below. In state 1, the contact force F_n is given by:

$$F_n = k_n^1 \cdot \delta_n, \quad (1)$$

¹ <https://yade-dem.org/wiki/Yade>.

² Using a Hertzian spring formulation would have been theoretically more accurate for the elastic part, but the use of a linear spring leads to faster computations with similar results because contact forces remain small (Silbert et al. (2001)).

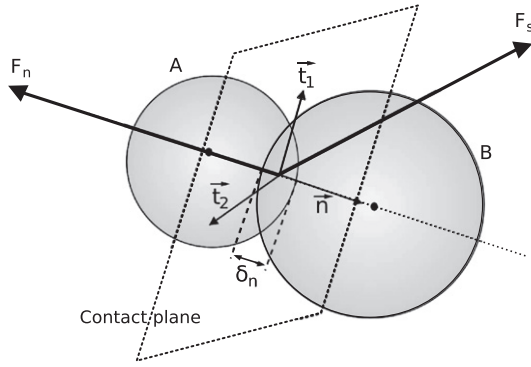


Fig. 1. Two elements A and B are in contact when an overlap δ_n occurs between them. The definitions of the normal direction n and tangential directions t_1 and t_2 are relative to the contact plane.

where δ_n is the normal overlap and k_n^1 is the elastic contact stiffness defined as:

$$k_n^1 = 2 \cdot \frac{k_n^A k_n^B}{k_n^A + k_n^B}, \quad (2)$$

which is the harmonic average between the local k_n^A and k_n^B , which are the local stiffnesses associated with elements A and B respectively, and are defined as $k_n^i = E^i \cdot R^i$ ($i = A, B$) with R^i being the radius of particle i and E^i being a local parameter (In case of a contact between a particle and a box, the box infinite radius is replaced by the particle radius to compute the local stiffness.).

States 2 and 3 correspond to a hysteretic behaviour, for which the resulting energy dissipation is conditioned by the value of a restitution coefficient e_n , defined by the ratio between initial and final relative normal velocities for a binary contact. Using this definition and Newton's second law, the following relationship (demonstrated in Walton and Braun (1986)) is obtained:

$$e_n = \sqrt{\frac{k_n^1}{k_n^2}}, \quad (3)$$

from which the value of the hysteretic stiffness k_n^2 can be computed.

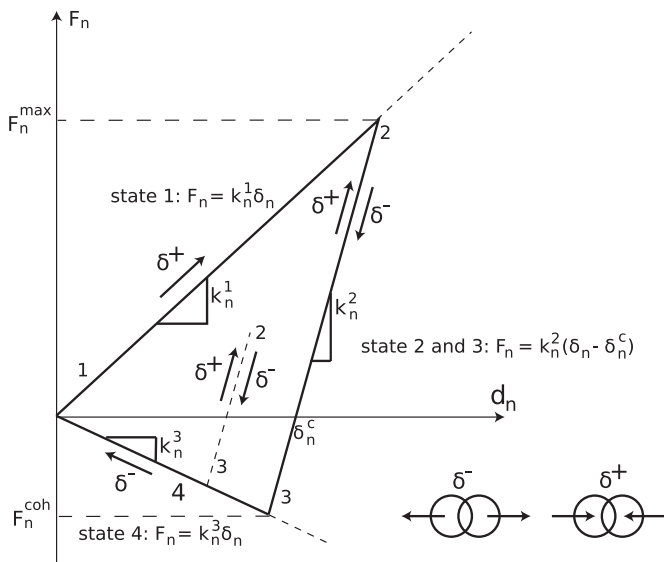


Fig. 2. Schematic graph of the piecewise elastic (state 1), hysteretic (states 2 and 3) and cohesive (states 3 and 4) normal contact model. k_n^1 , k_n^2 and k_n^3 are the corresponding stiffnesses. F_n^{\max} and F_n^{coh} are the maximum repulsive and attractive values that can be reached by the contact force, respectively. The upper right diagram represents a 2D view of the contact between two elements A and B, with an overlap δ_n .

To quantify the contribution of attractive forces, a normal cohesion coefficient α_c is defined by:

$$\alpha_c = \frac{|k_n^3|}{k_n^1}. \quad (4)$$

For a chosen normal cohesion coefficient, the value of the cohesive stiffness k_n^3 can be deduced.

When a new contact occurs, the contact force initiates from state 1. The value of the maximum contact force F_n^{\max} depends on the initial relative velocity between the two elements under consideration. This value is saved for the whole duration of the contact, and it can be updated. Starting from state 1, when F_n reaches F_n^{\max} , the contact goes into state 2, and the value of δ_n^c is computed during the transition between these two states. From state 2, if both elements get closer, there are two options. If $k_n^1 \delta_n$ is higher than $k_n^2 (\delta_n - \delta_n^c)$ then the contact remains in the same state, otherwise the contact goes back to state 1 which may lead to a change in F_n^{\max} . From state 2, if both elements move away from each other, the resulting state depends on the sign of $k_n^2 (\delta_n - \delta_n^c)$. If it is positive, the contact remains in state 2, whereas if it is negative, the contact changes to state 3.

Following the normal contact model, during the attractive phase (states 3 and 4), when the contact is in state 3 and both elements are getting closer, the contact goes back to state 2 if $k_n^2 (\delta_n - \delta_n^c)$ is positive, or remains in state 3 if it is negative. Otherwise, both elements are moving away from each other, and the next state depends on the sign of $k_n^2 (\delta_n - \delta_n^c) - k_n^3 \delta_n$. If positive, the contact remains in state 3, whereas if it is negative, the contact moves to state 4 and δ_n^c is updated to a lower value (as for F_n^{\max} and F_n^{coh}). From state 4, the contact either goes back to state 3 if both elements get closer again, and the contact force is then $k_n^2 (\delta_n - \delta_n^c)$ (computed from the updated value of δ_n^c), or it remains in state 4 otherwise. The contact finally disappears when $\delta_n < 0$.

2.1.2. Tangential contact: Frictional cohesive model

The tangential contact model corresponds to a regularised Coulomb's friction law with tangential cohesion (see Fig. 3). Fig. 3a shows the shear strength $F_{s,\max}$ as a function of the normal contact force, and Fig. 3b shows the tangential force F_s actually computed for a fixed value of the normal contact force. A tangential stiffness is involved in the regularisation, it is defined as:

$$k_s^i = 2 \cdot \frac{\nu^A k_n^A \cdot \nu^B k_n^B}{\nu^A k_n^A + \nu^B k_n^B} \times \xi_i, \quad (5)$$

where ν^A and ν^B are Poisson's ratio, and ξ_i is a numerical coefficient depending on the normal contact model. The value of the subscript i depends on the normal contact state: it is 1 for the elastic state (for which $\xi_{i1} = 1$), it is 2 for the hysteretic state (for which $\xi_{i2} = k_n^2/k_n^1$) and it is 3 for the cohesive state (for which $\xi_{i3} = |k_n^3/k_n^1|$).

As shown in Fig. 3a, when the normal cohesion is computed with the normal contact model, tangential cohesion is also computed with the tangential contact model. Consequently, it is the normal cohesion that induces cohesion in the model, at both the local and the global scales. In the rest of the paper, for the sake of clarity, we will reserve the word cohesion to the macroscopic scale. Wherever it is more relevant to consider the microscopic scale, we will refer to normal cohesion or tangential cohesion.

3. Description and setup of the granular launcher

In a previous work, Favier et al. (2009) modelled a whole impact flow experiment, starting from the upstream triggering of the granular material at null velocity, and ending with the downward impact event on the obstacle. Based on this “standard” model, we were able

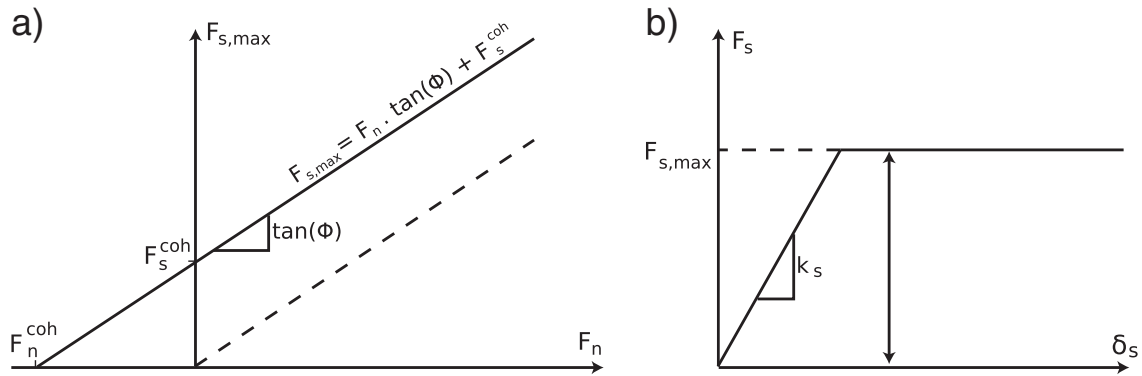


Fig. 3. Frictional and cohesive tangential contact model. The tangential cohesion F_s^{coh} arises from the normal cohesion F_n^{coh} computed with the normal contact model, and the friction angle ϕ . a) Shear strength. The case of a non-cohesive material is shown in dashed lines. b) The tangential contact force as a function of the tangential relative displacement is computed using a regularised Coulomb's friction law.

to compute the drag coefficient from internal characteristics of the flow. However, due to the high calculation cost of this comprehensive approach, it was not possible to perform extensive parametric studies. Therefore, we propose here an efficient numerical tool, calibrated from the standard model, to overcome this limitation.

3.1. Granular launcher principle and setup

The numerical tool, called “granular launcher”, is presented in Fig. 4. The setup of the granular launcher requires four initial input parameters: the launching distance D_i , which is the distance separating the downstream obstacle from the location from which the particles will be thrown, the initial flow velocity V_i which is uniform, the initial flow density ρ_i and thickness h_i . The initial sample is generated by creating a non-cohesive granular assembly by gravity deposition in a parallelepipedic box (which has the same width as the canal). The deposition process is over when the chosen initial density is reached (the residual kinetic energy is then low). Then, the upper part of the deposit is removed to match the chosen initial thickness, and a few vertical layers are removed at the sample front and back to avoid boundary effects on the granular flow experiments. During a simulation, all the particles located upstream from the launching distance are given an initial velocity V_i . Thus, the part of the granular assembly located in this area moves downward like a rigid body, without any internal deformations, while the downstream part flows under the effect of gravity.

With this method, only the flow/obstacle interaction is modelled, which reduces drastically CPU time for each simulation (from days to hours). Moreover, the initial conditions from which the drag coefficient is calculated are fully controlled, and can thus be modified in order to perform parametric studies.

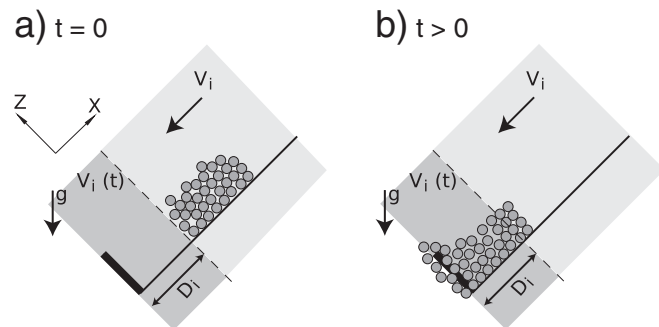


Fig. 4. Granular launcher principle. a) An initial granular sample (created by gravity deposit) is positioned at $x = D_i$, it has an initial velocity V_i , a density ρ_i , and a thickness h_i . b) During the simulation, the particles located upstream $x = D_i$ (background in light grey) are given a uniform initial velocity, whereas others undergo gravity (background in darker grey).

3.2. Validation of the granular launcher

The granular launcher is validated by comparing the amplitude of the obstacle load with the results produced by the standard model, during the steady regime and for a non-cohesive granular flow (equivalent to $\alpha_c = 0$). The transient regime, characterised by both non-steady flow properties and obstacle load (this definition will be detailed in Section 1), is not considered because it depends on the bulk properties at the front of the granular assembly, which are totally different between the standard model (see Favier et al. (2009)) and the granular launcher.

The following parameters are used. The slope angle is 43° from the horizontal and the canal is 20 cm wide. The obstacle is a $c = 4$ cm side square, positioned perpendicular to the (x, y) plane and centred in the central flowline. The mean radius of the spherical particles is 2.5 mm, with a scattering of 2%. The values of the micromechanical contact parameters are presented in Table 1. These values are similar to the ones used in a previous work (detailed in Favier et al. (2009)).

The values chosen for E and ν correspond to a fairly smooth material, with typical overlaps of around one percent of the particle radius. The reason of this choice is due to the relationship between stiffnesses and the time step of the simulations, which prohibits any large-scale study if the stiffness is too high. More important, this choice is justified by the good fit obtained previously between the standard model and the original laboratory experiments (again see Favier et al. (2009)) with the same numerical contact properties, although the experimental material was made of spherical glass particles, having a significantly larger stiffness. Note that a few studies have already shown an agreement between flow properties from simulations and experiments (Hanes and Walton, 2000; Taberlet, 2005).

Table 1

(a) Types of discrete elements and their micromechanical properties. Particles are spherical and moving elements, while boxes are parallelepipedic, fixed elements and represent either the obstacle or a wall. (b) Contact properties between the different types of elements. These values are constant for all the results presented in the paper.

Element type	Particle	Obstacle	Wall	
E (N.m ⁻²)	10 ⁷	10 ⁷	10 ⁷ /26	
ν	0.21	0.34	0.31	
Density (kg.m ⁻³)	2500			
Radius (mm)	5 (+/- 2%)			
(a)				
	Contact particle/..	Particle	Obstacle	Wall
Normal contact	k_n^1 (N.m ⁻¹)	25,000	25,000	964
	e_n	0.5	0.5	0.5
Tangential contact	k_s^1 (N.m ⁻¹)	5250	6490	566
	ϕ (°)	30	18	19
(b)				

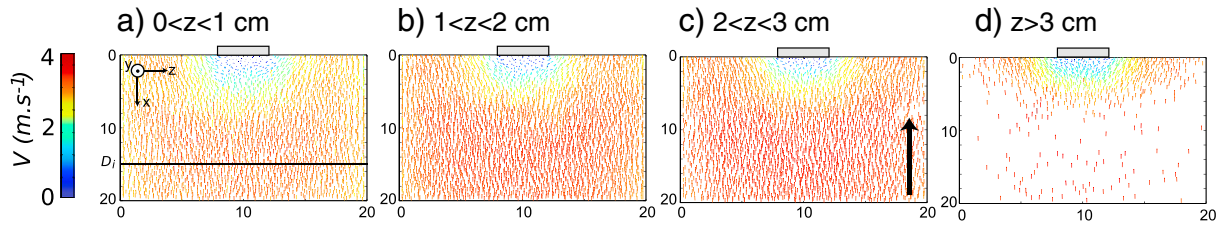


Fig. 5. 2D projections of particle velocities in the (x,y) plane of 1 cm thick horizontal layers, from $z=0$ to $z=4$ cm, for the standard model. a) Basal section ($0 < z < 1$ cm), b) and c) intermediate sections ($1 < z < 3$ cm) and d) top section ($z > 3$ cm). The assumed value of D_i is represented in a) by a horizontal line.

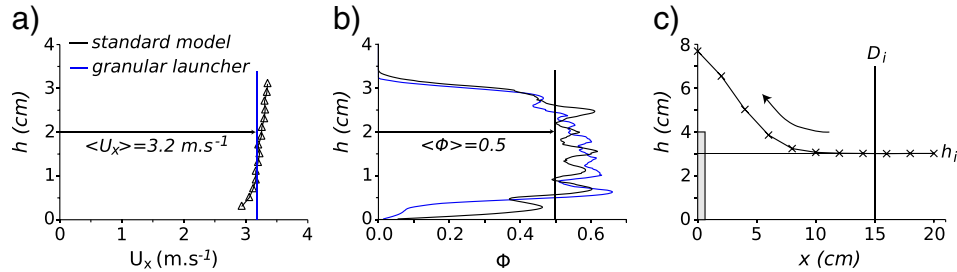


Fig. 6. Vertical a) velocity and b) solid fraction profiles in the canal central part for $x = D_i = 15$ cm obtained with the standard model (black curves) and adapted for the validation of the granular launcher (blue curves). Both curves of each graph in a) and b) have similar average values (shown by the vertical lines). c) Height of the free surface in the central flowline with the standard model. (For interpretation of the references to colour in this figure legend, the reader is referred to the web version of this article.)

for similar particle sizes and contact stiffnesses. An explanation of this could be that the energy transmitted by a particle to the obstacle during an impact is constant whatever the stiffness, the maximum load being balanced by the duration of the contact. Applying a moving average to the load during the steady regime thus leads to a similar amplitude whatever the particle stiffness considered.

The granular launcher is validated with the following initial parameters. The launching distance is chosen to be higher than the obstacle influence zone on the granular flow, deduced from the standard model. This distance is assessed with the 2D projections of particle velocities in the (x,y) plane for 1 cm high horizontal layers obtained with the standard model (plotted in Fig. 5). Here, $D_i = 15$ cm is chosen for the launching distance (represented by a horizontal line as shown in Fig. 5a).

The vertical velocity and density profiles on the central part of the canal obtained with the standard model are represented at $x = D_i$ in Fig. 6a and b. The initial velocity and density are chosen to be equal

in average to their values from the standard model, i.e. $V_i = 3.2 \text{ m.s}^{-1}$ and $\rho_i = 1250 \text{ kg.m}^{-3}$. The initial thickness equals the thickness obtained at $x = D_i$, which is $h_i = 3.05$ cm according to Fig. 6c.

The resulting load applied on the obstacle is plotted in Fig. 7. It was smoothed by applying a moving average to the raw results (a moving average was also applied to the results of the standard model, see Favier et al. (2009)). During the steady regime, the averaged load equals 15.5 N, which is slightly higher than the value of 14.7 N obtained with the standard model. This deviation is sufficiently low to validate the granular launcher.

4. Effect of a cohesive granular flow on the drag coefficient

We investigated the drag coefficient of an obstacle impacted by a cohesive granular flow, for a supercritical range of Froude numbers. First of all, we examine the effect of cohesion on the obstacle load, and then we perform a more complete analysis of its coupled effect with the Froude number on the drag coefficient.

4.1. Effect of cohesion

Cohesion is induced by the cohesive coefficient implemented in the normal contact model (see Section 2). Here we explore the effect of a variation of this normal cohesive coefficient α_c on the obstacle load. α_c ranges from 0 (non-cohesive flow) to 1 (highly-cohesive flow), and the other parameters of the study are detailed in Table 2.

Table 2

Initial values used for the granular launcher to estimate the influence of cohesion on the obstacle load (they differ from those used in the validation procedure, see Section 3). The elements and contact parameters are similar to those mentioned in Table 1.

Parameter	Symbol	Value
Launching distance	D_i	15 cm
Initial velocity	V_i	3 m.s^{-1}
Froude number	Fr	5.85
Initial thickness	h_i	4 cm
Initial flow density	ρ_i	1250 kg.m^{-3}
Normal cohesion coefficient	α_c	0 to 1

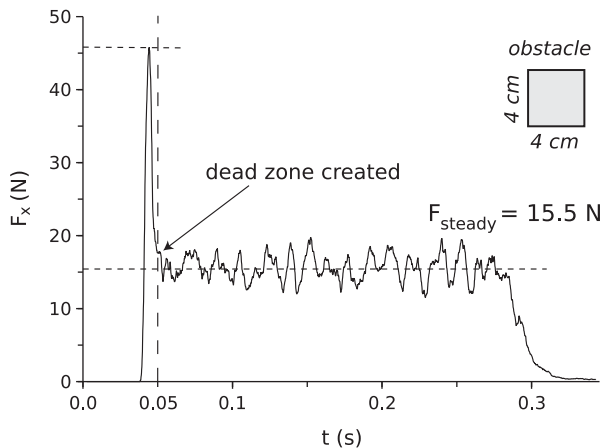


Fig. 7. Resulting smoothed load (The temporal width of the moving average is 0.005 s) undergone by the obstacle during the validation of the granular launcher. Both the transient and steady regimes clearly appear. During the steady regime, the average load equals 15.5 N whereas it was equal to 14.7 N for the standard model (see Favier et al. (2009) for more details about the standard model results). The overestimation is in the order of a few percent, thus this experiment validates the granular launcher.

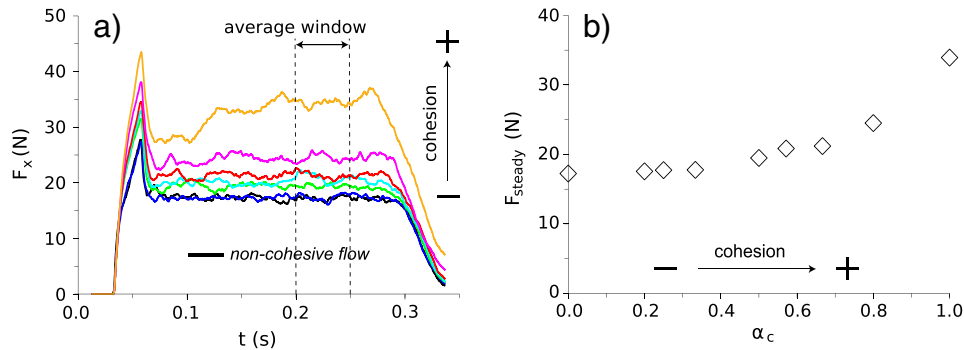


Fig. 8. Effect of cohesion (controlled with the normal cohesion coefficient α_c) on the obstacle load. a) Smoothed load (The temporal width of the moving average is 0.025 s) profiles for a series of normal cohesion coefficients between 0 and 1. The case where $\alpha_c = 0$ is represented in black. The steady state load is computed within the average window between both vertical dashed lines. b) Steady load as a function of α_c . (For interpretation of the references to colour in this figure legend, the reader is referred to the web version of this article.)

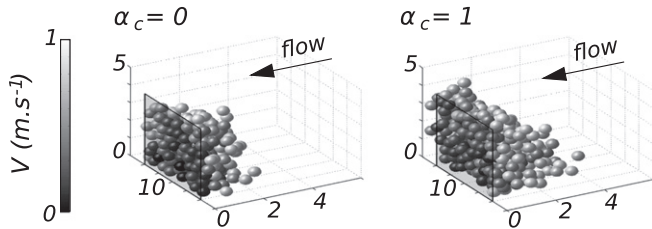


Fig. 9. Increasing cohesion (see Table 2) increases the size of the dead zone, which here covers the area where particle velocity is less than 1 m.s⁻¹.

4.1.1. Cohesion effect on the obstacle load

The smoothed temporal profiles of the obstacle loads are plotted in Fig. 8a. As described earlier by Tai et al. (2002), Gray et al. (2003) or Pudasaini and Kröner (2008), in each curve the transient regime is characterised by a rapid increase of the initial load (see short load peaks in Fig. 8a) followed by the upslope propagation of a shock wave, seen as a sharp discontinuity of the free surface characterised by an upward velocity decrease and a thickness increase. During the transient regime, a dead zone composed of low-velocity particles forms upstream the obstacle (our dead zone has a half-cylinder shape similar to the one obtained by Teufelsbauer et al. (2009), see Fig. 5). By the time the dead zone is fully formed, the granular flow enters the steady regime and the load rapidly decreases to reach its steady state value. The steady regime is then associated with smoother spatial variations of the free surface, which is a consequence of a nearly stagnant zone (the dead zone) coexisting with an inertial zone above composed of particles deviated by the dead zone (as also described by Faug et al. (2009, 2011) and Chanut et al. (2010)) for a wall spanning the whole width of the canal.

The steady state load is computed as a function of the normal cohesive coefficient in Fig. 8b: its value is nearly constant until $\alpha_c = 0.5$ is reached, then it increases smoothly to finally double for the most cohesive flow.

4.1.2. Cohesion effect on the flow parameters

Here, the dead zone refers to the area where particle velocity is less than 1 m.s⁻¹, which is about one third of the initial velocity (the resulting dead zone can be observed in Fig. 5 in dark blue). As shown in Fig. 9, the volume of the dead zone increases with the amount of cohesion, which is also a consequence of the global decrease in the bulk velocity.

The solid fraction vertical profiles in the central part are represented as functions of height for $x = 5$ cm (see Fig. 10a) and $x = 10$ cm (see Fig. 10b). These profiles are smoothed to facilitate comparisons between curves. An increase of the cohesion induces an increase of the thickness near the obstacle (at $x = 5$ cm), along with a decrease of the solid fraction. This could be explained by the fact that cohesive flows behave non-homogeneously, as evidenced by the many empty spaces between clusters of particles as mentioned by Rognon et al. (2008b), which lowers the solid fraction.

The high increase of the obstacle load observed for an increase in cohesion cannot be related to the changes of bulk velocity and solid fraction, because they both decrease slightly. Thus, we now focus on the possible contribution of the contact force network, and how it evolves in relation to cohesion changes.

4.1.3. Cohesion effect on the contact force network

The effect of increasing the normal cohesion coefficient is to increase the attractive forces in the granular assembly. This leads to an increase of the contact persistency and consequently to an increase in the

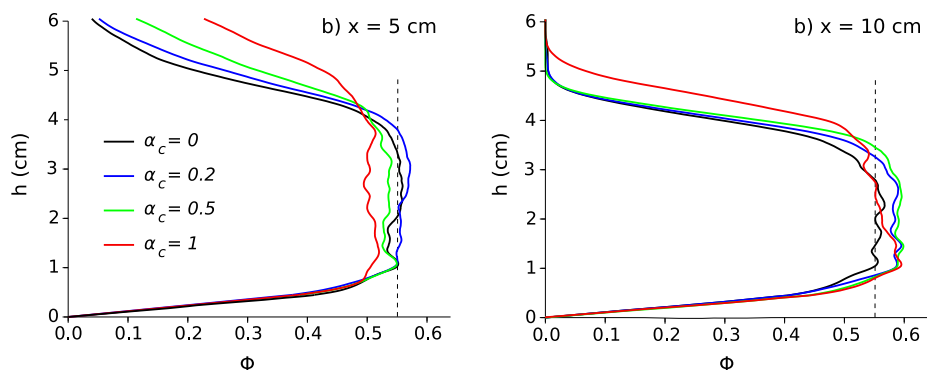


Fig. 10. Solid fraction vertical profiles in the central part as a function of height, for various cohesions, 5 cm (left side) and 10 cm (right side) from the obstacle. The profiles are smoothed using a moving average to facilitate comparisons between curves.

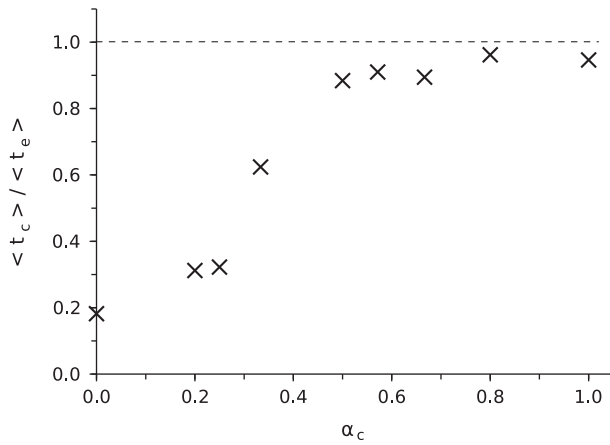


Fig. 11. Ratio between the mean duration of contacts $\langle t_c \rangle$ and the mean time to go through the flow zone $\langle t_e \rangle$ as a function of the normal cohesion coefficient. Averages are computed from 10 particles uniformly distributed inside the flow zone.

number of contacts. This is illustrated in Fig. 11, where the ratio between the mean duration of contacts $\langle t_c \rangle$ and the mean time taken by a particle to cross the flowing area $\langle t_e \rangle$ (i.e., between $x = D_i$ and $x = 0$ cm) is plotted. In a non-cohesive flow, a contact lasts an average of one fifth the average time taken to cross the flowing area, whereas for a highly-cohesive flow, the ratio is close to 1, indicating that most of the contacts are rapidly created and do not break easily. The ratio tends towards 1 when the normal cohesion coefficient is higher than 0.5, which is also the value from which the obstacle load increases in Fig. 8b, indicating that the duration of intergranular force chains is of great influence.

The higher contact persistency corresponds to a higher number of contact per particle, i.e. the coordination number C (defined as the ratio between the number of contacts divided by twice the number of particles). The coordination is plotted in Fig. 12 as a function of the distance to the obstacle. Whatever the bulk cohesion, the coordination increases in the vicinity of the obstacle. This may suggest that the weight of the dead zone could contribute to the obstacle load. Nevertheless, with our dead zone criteria, the contribution of the dead zone represents at most 2% of the load whatever the cohesion level.

Fig. 12 shows also that coordination increases as cohesion increases. When the granular assembly is non-cohesive, C ranges from 1 to 2, indicating that the contact network is very loose. An immediate consequence is a weak propagation of the contact force through discrete particles. When cohesion increases, C rapidly increases from around 3

(for $\alpha_c = 0.2$ and 0.5) to reach 4 for $\alpha_c = 1$. For the latter, each particle is thus in contact with at least 3 other particles on average and the contact force transmission inside the granular volume is more efficient. This suggests that a better transmission of the normal contact forces inside the granular assembly contributes to the observed increase of the obstacle load (again, see Fig. 8).

The increase of the obstacle load is also in good agreement with Fig. 13, which shows the normal contact force network upstream the obstacle. The contact network is made up of the numerous small bonds representing the normal contact forces that link the centres of two particles in contact. Their colour corresponds to the state in which the contact stands (see Section 2), and their thickness is a linear function of the normal contact force intensity. When $\alpha_c = 0$, there is no normal cohesion so the green colour disappears, and the brown colour thus corresponds to a null contact force with a residual overlapping. Fig. 13 shows again that adding cohesion to the granular assembly has a key role in the densification of the contact network, which is related to an increase of the contact chain persistency and an increase of the coordination. To conclude, it is likely that these modifications in the contact network are responsible for the increase of the obstacle load.

4.2. Coupled effect of cohesion and Froude number

4.2.1. Definitions and previous studies

The Froude number Fr is defined as the ratio of flowing material inertia to gravitational forces, such that:

$$Fr = \frac{V_i}{\sqrt{gh_i}}, \quad (6)$$

where $g = 9.81 \text{ m.s}^{-2}$ is the gravity acceleration. The drag coefficient C_d is the ratio of the load applied on the obstacle to the dynamic pressure inside the flow and it is given by:

$$C_d = \frac{F_x}{c^2 \frac{1}{2} \rho_i V_i^2}, \quad (7)$$

with c^2 being the surface area of the obstacle and F_x the drag force applied on the obstacle.

Some other studies made on a sufficiently wide range of Froude numbers present the evolution of C_d as a power law function of Fr , such that:

$$C_d = a Fr^{-b}, \quad (8)$$

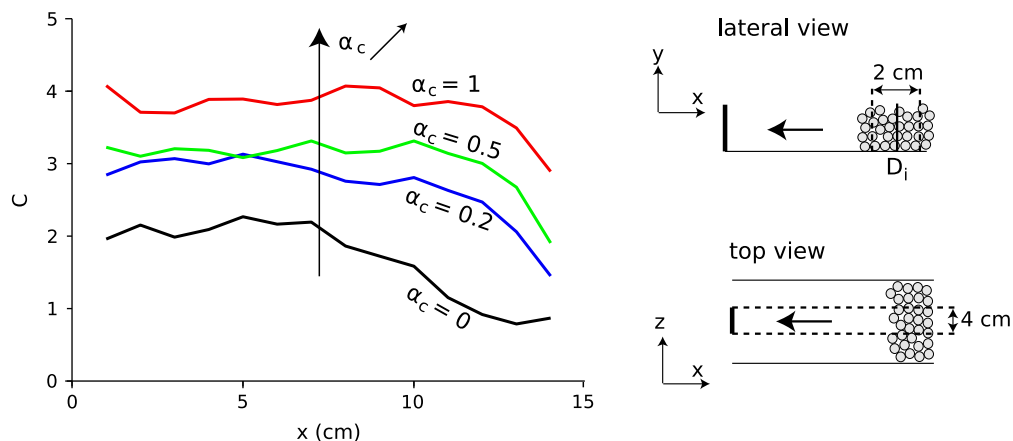


Fig. 12. Coordination number C as a function of the distance upstream the obstacle, for various normal cohesion coefficients. C is computed during the steady regime inside the volume described in the diagram on the right.

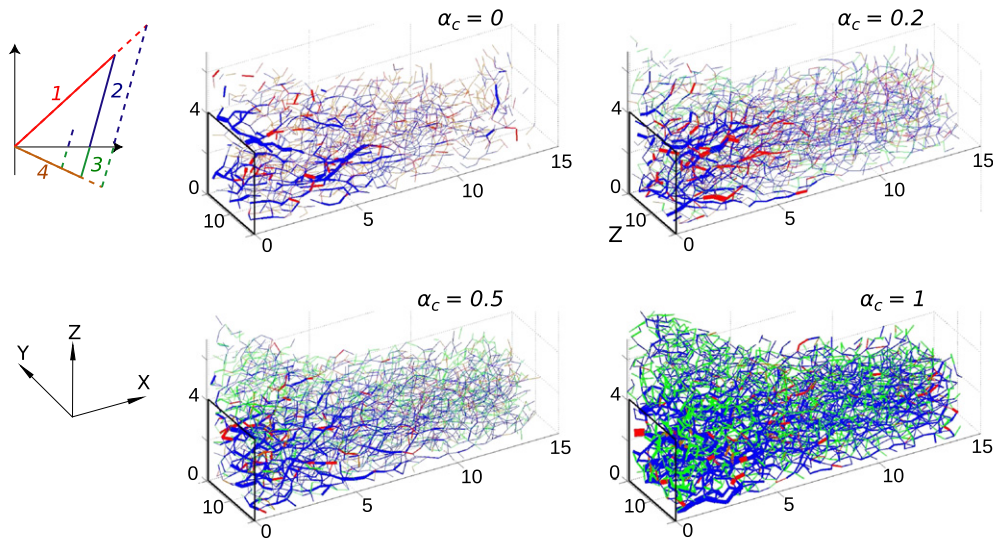


Fig. 13. 3D view of the normal contact force network. The colour code corresponds to the contact states (top left, as described in Section 2). For clarity reasons, only contacts located directly upstream the obstacle are represented (i.e. the lateral corridors are not represented). (For interpretation of the references to colour in this figure legend, the reader is referred to the web version of this article.)

where a and b are empirical coefficients (Baroudi and Thibert, 2009; Chehata et al., 2003; Thibert et al., 2008).

The granular launcher was validated for $Fr = 5.85$, therefore the same order of magnitude is used for the present parametric study. When Fr is lower than 1.5, due to gravity, the granular flow collapses before impacting the obstacle with no possibility to calculate any drag coefficient. Thus, the initial velocity V_i is chosen in the range $0.94\text{--}7.01\text{ m.s}^{-1}$, which corresponds to Fr in the range 1.5–11.2. The other initial parameters of the granular launcher, the thickness h_i , the flow density ρ_i , the launching distance D_i and the normal cohesion coefficient α_c are given in Table 2.

4.2.2. Results and discussion

The results of the parametric study are presented in Fig. 14 in the form of the drag coefficient as a function of the Froude number. We used a double logarithmic scale to facilitate the comparisons with the

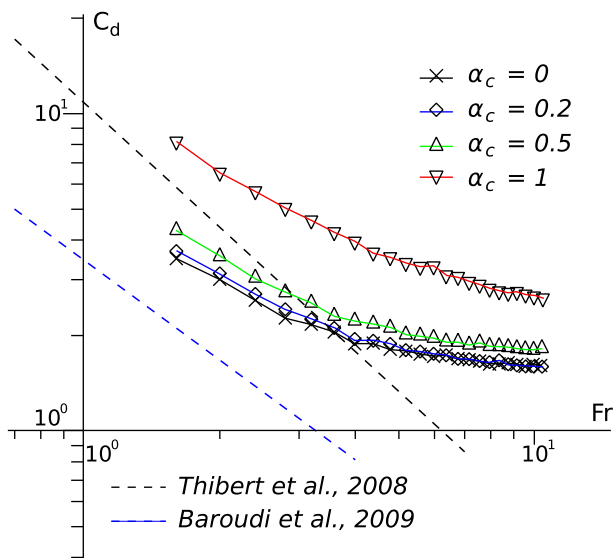


Fig. 14. Drag coefficient as a function of the Froude number, for various cohesions. A double logarithmic scale is adopted. Analogous results from Thibert et al. (2008) and Baroudi and Thibert (2009) are also plotted (dashed lines).

power law used in the literature (see Eq. 8). The results from Thibert et al. (2008) and Baroudi and Thibert (2009) are also represented.

As previously obtained for $Fr = 5.85$ (see Section 3), the drag coefficient increases with the bulk cohesion, for the whole range of Froude numbers. The curves are nearly parallel, except for a slight deviation for $\alpha_c = 1$ with the other curves for high Froude numbers. For a non-cohesive flow, C_d ranges from 1.5 to 3.3, whereas for a highly-cohesive flow, C_d increases largely from 2.5 to 8.

All the curves exhibit a convex decrease when the Froude number increases. This convexity seems to show that the use of a power law to establish a relationship between the drag coefficient and the Froude number should consider a non-constant value for the power law exponent b , when the range of Froude numbers is sufficiently wide. This is because when Fr is close to 0 (i.e. subcritical flows), the flow is mainly controlled by gravitational forces. For this regime, studies have shown that the drag is independent of the flow velocity (see Wieghardt (1974) for a cylinder moving inside a media composed of sand, Albert et al. (1999) and Chehata et al. (2003) for a granular flow made of granular spherical particles, and for full-scale snow avalanche experiments in Sovilla et al. (2008a)). This regime then corresponds to Eq. 8 associated with $b = 2$, which gives $F_x = 1/2ac^2 \cdot \rho g h_i$, without inertial terms which have vanished. When Fr increases from subcritical to supercritical regimes, the flow is increasingly controlled by inertial forces rather than gravitational forces. In this regime, Thibert et al. (2008) and Baroudi and Thibert (2009) performed in-situ experiments and obtained the relation $C_d = 10.8Fr^{-1.3}$ and $C_d = 3.6Fr^{-1.1}$ respectively for Froude numbers between about 0.5 and 6. Thus, it seems that not only the drag coefficient decreases with the Froude number, but also the contribution of inertial effects increases and consequently the contribution of gravitational effects decreases.

For the smallest values of Fr investigated, the exponent of the power law is very similar whatever the cohesion, around 0.7. This is not equal to the in-situ curves, but the convexity of our curves suggests that our power law exponent would have tended to be higher if the Froude number had been lower. Thus, our results are in agreement with those of Thibert et al. (2008) and Baroudi and Thibert (2009) for low Froude numbers around 1. Moreover, an extension of our curves seems to lead to drag coefficient of at least 10 for the subcritical regimes and for a highly-cohesive flow, while for a non-cohesive flow, the values are more in agreement with the maximum value recommended by Norem (1990). On the other hand, for the highest Froude numbers,

we found higher values of C_d comparatively to the in-situ curves, and our power law exponent tends towards 0 (for $Fr = 11.2$, the exponent is between 0.06 for a highly-cohesive flow and 0.32 for a non-cohesive flow).

For any value of the Froude number, cohesion has a strong effect on the drag coefficient as long as the normal cohesion $\alpha_c > 0.5$ (see Fig. 8b). This threshold also corresponds to the value above which the intergranular force chains never break up (see Fig. 11). The formation and destruction of the force chains within snow material were identified as a possible cause explaining the high fluctuations of load pressure applied by wet-snow avalanches on a pylon (Baroudi et al., 2011; Sovilla et al., 2010). This conclusion is supported by numerical modelling of slow drag motion around an obstacle using discrete models (Geng and Behringer, 2005). Besides, Sovilla et al. (2010) and Baroudi et al. (2011) also obtained high values of the drag coefficient, much higher than the ones expected using the predictions of conventional avalanche engineering guidelines, which could be related to the forming of these force chains.

According to our results, the increase of cohesion densifies the contact network which increases the contact chains' persistency as well. Therefore, intergranular contact forces are easily transmitted between discrete particles and can propagate to the obstacle, with a resulting increase of the drag coefficient.

5. Conclusion

In the present study, a numerical tool based on a discrete element method was developed to simulate the impact of a granular flow on an obstacle. Our model enables us to conduct extensive parametric studies with fully controlled initial flow parameters, such as velocity, density and thickness. Controlling the initial flow leads to an accurate computation of the drag coefficient, which is the ratio between the load applied on the obstacle and the dynamic pressure.

The micromechanical laws take into account a cohesive elastoplastic normal component and a cohesive frictional tangential component. The effect of cohesion on the load undergone by the obstacle was investigated. In a substantial way, the higher the cohesion, the higher the load. According to our model, this is due to a densification of the contact network and an increase of the contact chains persistency, which facilitate the propagation of the normal contact forces inside the flowing granular material towards the obstacle surface, and contribute to increase its load.

The coupled effect of cohesion with the Froude number on the drag coefficient was also investigated. A strong effect of cohesion on the drag pressure was observed, for all Froude numbers tested (ranging from 1.5 to 11.2). Our study also shows an increased influence of the gravitational forces over inertial forces as the Froude number decreases, for all values of cohesion. This means that the drag coefficient needs to be considered as a power law function of the Froude number with a non-constant value of the power law exponent. It has been shown that this exponent depends on the ratio between inertial and gravitational effects.

The drag coefficient considered in the construction of avalanche protection structures depends simply on the obstacle shape, and on the moisture content of the flowing avalanche. However, it doesn't account for snow cohesion whereas it obviously exists within snow avalanches, and is thought to have significant consequences for wet-snow avalanches. Indeed, according to our study, for Froude numbers between 1 and 2, the drag undergone by the obstacle could be three times higher for a highly-cohesive granular flow comparatively to a non-cohesive flow. The values obtained for the drag coefficient were higher than the highest one recommended by Norem (1990), and the convex curvature of our numerical results suggests that they could be much higher for subcritical regimes, typical of wet-snow avalanches. This strongly suggests that snow cohesion is lacking and should be of great interest to provide better estimates of the drag coefficient used by the protection structure designers.

Acknowledgements

We would like to acknowledge the ANR (National Research Agency) project OPALE (Ouvrages de Protection et bâtiments pavillonnaires soumis l'Action des avalanches), and the Cluster environment, in the Rhône-Alpes region, for their financial support.

References

- Albert, R., Pfeifer, M., Barabási, A., Schiffer, P., 1999. Slow drag in a granular medium. *Physical Review Letters* 82, 205–208.
- Barbolini, M., Biancardi, A., Natale, L., Pagliardi, M., 2005. A low cost system for the estimation of concentration and velocity profiles in rapid dry granular flows. *Cold Regions Science and Technology* 43, 49–61.
- Barbolini, M., Domaas, U., Faug, T., Gauer, P., Hakonardottir, K., Harbitz, C., Issler, D., Johannesson, T., Lied, K., Naaim, M., Rammer, L., 2009. The design of avalanche protection dams. Recent practical and theoretical developments. European Commission, Climate Change and Environmental Risks. 212 p.
- Baroudi, D., Thibert, E., 2009. An instrumented structure to measure avalanche impact pressure: error analysis from Monte Carlo simulations. *Cold Regions Science and Technology* 59, 242–250.
- Baroudi, D., Sovilla, B., Thibert, E., 2011. Effects of flow regime and sensor geometry on snow avalanche impact-pressure measurements. *Journal of Glaciology* 57, 277–288.
- Bartelt, P., McDell, B., 2009. Granulometric investigations of snow avalanches. *Journal of Glaciology* 55, 829–833.
- Berthet-Rambaud, P., Limam, A., Baroudi, D., Thibert, E., Taillandier, J., 2008. Characterization of avalanche loading on impacted structures: a new approach based on inverse analysis. *Journal of Glaciology* 54, 324–332.
- Chanut, B., Faug, T., Naaim, M., 2010. Time-varying force from dense granular avalanches on a wall. *Physical Review E* 82, 041302.
- Chehata, D., Zenit, R., Wassgren, C., 2003. Dense granular flow around an immersed cylinder. *Physics of fluids* 15, 1622.
- Cundall, P., Strack, O., 1979. A discrete numerical model for granular assemblies. *Geotechnique* 29, 47–65.
- De Biagi, V., Chiaia, B., Frigo, B., 2012. Fractal grain distribution in snow avalanche deposits. *Journal of Glaciology* 58, 587–592.
- Faug, T., Beguin, R., Chanut, B., 2009. Mean steady granular force on a wall overflowed by free-surface gravity-driven dense flows. *Physical Review E* 80, 021305.
- Faug, T., Caccamo, P., Chanut, B., 2011. Equation for the force experienced by a wall overflowed by a granular avalanche: experimental verification. *Physical Review E* 84, 051301.
- Favier, L., Daudon, D., Donzé, F., Mazars, J., 2009. Predicting the drag coefficient of a granular flow using the discrete element method. *Journal of Statistical Mechanics: Theory and Experiment* 2009, P06012.
- Gauer, P., Issler, D., Lied, K., Kristensen, K., Iwe, H., Lied, E., Rammer, L., Schreiber, H., 2007. On full-scale avalanche measurements at the Ryggfönn test site, Norway. *Cold Regions Science and Technology* 49, 39–53.
- Geng, J., Behringer, R., 2005. Slow drag in two-dimensional granular media. *Physical Review E* 71, 011302.
- Gray, J., Tai, Y., Noelle, S., 2003. Shock waves, dead zones and particle-free regions in rapid granular free-surface flows. *Journal of Fluid Mechanics* 491, 161–181.
- Hanes, D., Walton, O., 2000. Simulations and physical measurements of glass spheres flowing down a bumpy incline. *Powder Technology* 109, 133–144.
- Hauksón, S., Pagliardi, M., Barbolini, M., Johannesson, T., 2007. Laboratory measurements of impact forces of supercritical granular flow against mast-like obstacles. *Cold Regions Science and Technology* 49, 54–63.
- Jop, P., Forterre, Y., Pouliquen, O., 2005. Crucial role of sidewalls in granular surface flows: consequences for the rheology. *Journal of Fluid Mechanics* 541, 167–192.
- Kozicki, J., Donzé, F., 2008. A new open-source software developed for numerical simulations using discrete modeling methods. *Computer Methods in Applied Mechanics and Engineering* 197, 4429–4443.
- Luding, S., 2008. Cohesive, frictional powders: contact models for tension. *Granular Matter* 10, 235–246.
- Luding, S., Manetsberger, K., Müllers, J., 2005. A discrete model for long time sintering. *Journal of the Mechanics and Physics of Solids* 53, 455–491.
- Ma, Y., Thibert, E., Perrotin, P., Mommessin, M., 2009. Actions of snow avalanches on a snow shed. *Proceedings of the International Snow Science Workshop*, pp. 543–547.
- McClung, D., Schaerer, P., et al., 1985. Characteristics of flowing snow and avalanche impact pressures. *Annals of Glaciology* 6, 9–14.
- Mellor, M., 1968. Avalanches. *Cold Regions Science and Engineering*, Part III, Section A3D. US Army Cold Regions Research and Engineering Laboratory, Hanover, New Hampshire, USA.
- Moriguchi, S., Borja, R., Yashima, A., Sawada, K., 2009. Estimating the impact force generated by granular flow on a rigid obstruction. *Acta Geotechnica* 4, 57–71.
- Nishimura, K., Maeno, N., Sandersen, F., Kristensen, K., Norem, H., Lied, K., 1993. Observations of the dynamic structure of snow avalanches. *Annals of Glaciology* 18, 313–316.
- Norem, H., 1990. Ryggfönn-prosjektet. NGI Report 581200 16.
- Platzter, K., 2006. Experimental investigation of avalanche forces acting on snow sheds. Ph.D. thesis. University of Natural Resources and Applied Life Sciences Vienna.
- Pudasaini, S., Kröner, C., 2008. Shock waves in rapid flows of dense granular materials: theoretical predictions and experimental results. *Physical Review E* 78, 041308.
- Rognon, P., Chevoir, F., Bellot, H., Ousset, F., Naaim, M., Coussot, P., 2008a. Rheology of dense snow flows: inferences from steady state chute-flow experiments. *Journal of Rheology* 52, 729.

- Rognon, P., Roux, J., Naaïm, M., Chevoir, F., 2008b. Dense flows of cohesive granular materials. *Journal of Fluid Mechanics* 596, 21–47.
- Salm, B., Burkard, A., Gubler, H., 1990. Calcul des Avalanches: une méthode pour le praticien avec des exemples. *IFENA* 47, 38.
- Schaer, M., Issler, D., 2001. Particle densities, velocities and size distributions in large avalanches from impact-sensor measurements. *Annals of Glaciology* 32, 321–327.
- Schaerer, P., 1973. Observations of avalanche impact pressures. General Technical Report RM-3. US Dept. of Agriculture. Forest Service, pp. 51–54.
- Shen, H., Roper, A., 1970. Dynamics of snow avalanche (with estimation for force on a bridge). *Hydrological Sciences Journal* 15, 7–26.
- Silbert, L., Ertas, D., Grest, G., Halsey, T., Levine, D., Plimpton, S., 2001. Granular flow down an inclined plane: Bagnold scaling and rheology. *Physical Review E* 64, 051302.
- Sovilla, B., Schaer, M., Kern, M., Bartelt, P., 2008a. Impact pressures and flow regimes in dense snow avalanches observed at the Vallée de la Sionne test site. *Journal of Geophysical Research* 113, F01010.
- Sovilla, B., Schaer, M., Rammer, L., 2008b. Measurements and analysis of full-scale avalanche impact pressure at the Vallée de la Sionne test site. *Cold Regions Science and Technology* 51, 122–137.
- Sovilla, B., Kern, M., Schaer, M., 2010. Slow drag in wet-snow avalanche flow. *Journal of Glaciology* 56, 587–592.
- Taberlet, N., 2005. Ecoulements gravitaires de matériaux granulaires. Doctorat de l'Université de Rennes 1.
- Tai, Y., Noelle, S., Gray, J., Hutter, K., 2002. Shock-capturing and front-tracking methods for granular avalanches. *Journal of Computational Physics* 175, 269–301.
- Teufelsbauer, H., Wang, Y., Chiou, M., Wu, W., 2009. Flow-obstacle interaction in rapid granular avalanches: DEM simulation and comparison with experiment. *Granular Matter* 11, 209–220.
- Teufelsbauer, H., Wang, Y., Pudasaini, S., Borja, R., Wu, W., 2011. DEM simulation of impact force exerted by granular flow on rigid structures. *Acta Geotechnica* 1–15.
- Thibert, E., Baroudi, D., Limam, A., Berthet-Rambaud, P., 2008. Avalanche impact pressure on an instrumented structure. *Cold Regions Science and Technology* 54, 206–215.
- Valentino, R., Barla, G., Montrasio, L., 2008. Experimental analysis and micromechanical modelling of dry granular flow and impacts in laboratory flume tests. *Rock Mechanics and Rock Engineering* 41, 153–177.
- Voellmy, A., 1955. Ber die zerstörungskraft (on the destructive force of avalanches). *Schweizerische Bauzeitung* 73.
- Walton, O., Braun, R., 1986. Viscosity, granular-temperature, and stress calculations for shearing assemblies of inelastic, frictional disks. *Journal of Rheology* 30, 949.
- Wiegardt, K., 1974. Forces in granular flow. *Mechanics Research Communications* 1, 3–7.